Climate Dynamics (2003) 21: 647–658
DOI 10.1007/s00382-003-0358-9

L. D. D. Harvey

# Characterizing and comparing the control-run variability of eight coupled AOGCMs and of observations. Part 2: precipitation

Received: 17 December 2002 / Accepted: 20 August 2003 / Published online: 24 October 2003


**Abstract** This study examines the variability of annual-mean precipitation in eight AOGCMs and in observations using empirical orthogonal functions (EOFs). The leading mode of precipitation variability in both models and observations is centered around the low-latitude western Pacific Ocean and Indian Ocean, and is associated with the El Niño-Southern Oscillation (ENSO). The spatial pattern $R^2$ correlations between model and observed $EOF_1$ range from 0.12 to 0.61. In the observations, the Southern Oscillation Index (SOI) is highly correlated ($R^2 = 0.82$) with the amplitude of precipitation $EOF_1$, while model $R^2$ correlations range from 0.17 to 0.83. If grid points near to those used to compute the standard SOI are used to compute alternative SO indices, the correlation with the amplitude of $EOF_1$ ranges from 0.40 to 0.90 when based on the index that maximizes the correlation. Spatial fields of the variation between local precipitation and the SOI or the North Atlantic Oscillation Index are also computed for each model and compared with the observed fields. The model fields have many important similarities with the observed fields.

## 1 Introduction

In this work the interannual variability of global annual-mean precipitation fields as simulated by eight coupled, three-dimensional atmosphere ocean general circulation models (AOGCMs) is examined and compared with observed variability. This study complements Harvey and Wigley (2003; henceforth referred to as Part 1), who examined the observed and control-run variability of temperature for the same eight AOGCMs that are examined here. In that work, empirical orthogonal function (EOF) analysis is applied to the observed and model data. It was found that the principle model EOFs generally bear little resemblance to the principal observed EOFs, due in part to exaggerated model temperature variability at high latitudes and in part due to modes of variability that are in separate EOFs in the observations being partly mixed in a single EOF in the models. Motivated by the possibility that there could be modes of climate variability in the models corresponding, in terms of the underlying processes, to the principal modes of observed variability but not evident in the model EOFs, a "quasi-EOF" analysis technique was developed. The quasi-EOF analysis was designed to search for patterns of variability associated with the regions around which the observed modes of variability are centered.

In the case of precipitation, the primary global-scale mode of variability resembles the precipitation anomaly pattern associated with the El Niño-Southern Oscillation (ENSO), as does the first EOF derived from observed data (Dai and Wigley 2000). The second and third most important modes EOFs in both the model and observations are generally not statistically significant. Thus, there is no need to use the qEOF analysis to search for observed modes of variability within the model variability, so we restrict ourselves here to a comparison of the model and observed climatology and of $EOF_1$. Previous studies of the control-climate variability for a variety of models are summarized in Table 1 of Part 1.

As in Part 1, monthly data available from the Intergovernmental Panel on Climate Change (IPCC) Data Distribution Centre (DDC) website (http://ipcc-ddc.cru.uea.ac.uk/) for 200–240 years (depending on the model) of the control-run are used. The eight models analyzed, some of the properties of these models, and references in which the model simulation of the present-day climate is discussed are given in Table 1. Note that

L. D. D. Harvey
Department of Geography, University of Toronto,
100 St. George Street, Toronto M5S 3G3, Canada
E-mail: harvey@geog.utoronto.ca

**Table 1** The eight models analyzed here, length of the control run, the number of latitudes and longitudes for each model grid, and key references describing the models and the model spinup climate. Model or institutional acronyms are defined below Table 1

| Model | Length of control run (yrs) | Number of latitudes, longitudes | Flux-adjusted? | References |
|---|---|---|---|---|
| CCC | 200 | 48 × 96 | Yes | Flato et al. (2000) |
| CCSR | 210 | 32 × 64 | Yes | Emori et al. (1999) |
| CSIRO | 210 | 56 × 64 | Yes | Gordon and O'Farrell (1997), Walland et al. (2000) |
| ECHAM3 | 220 | 32 × 64 | Yes | Timmermann et al. (1999) |
| ECHAM4 | 240 | 64 × 128 | Yes | Bacher et al. (1998) |
| HadCM2 | 240 | 73 × 96 | Yes | Johns et al. (1997), Tett et al. (1997) |
| HadCM3 | 240 | 73 × 96 | No | Gordon et al. (2000), Collins et al. (2001) |
| PCM | 220 | 64 × 128 | No | Washington et al. (2000), Meehl et al. (2001) |

CCC, Canadian Climate Centre (Victoria, BC)
CCSR, Centre for Climate Research Studies (University of Tokyo)
CSIRO, Commonwealth Scientific and Industrial Research Organization (Australia)
ECHAM3 is the ECHAM3/LSG model, where ECHAM, *E*uropean *C*entre for Medium Range Weather Forecasts, University of *Ham*burg atmospheric model and LSG is a *L*arge *S*cale *G*eostrophic ocean model
ECHAM4 is the ECHAM4/OPYC3 model, where OPYC3 is an isopycnal-coordinate ocean model
HadCM2, Hadley Centre, Model 2 (Bracknell, UK)
HadCM3, Hadley Centre, Model 3 (Bracknell, UK)
PCM, Parallel Climate Model, National Center for Atmospheric Research (Boulder, Colorado)

all of the models except HadCM3 and PCM use flux adjustment to improve the simulation of average conditions for the present climate.

## 2 Statistical techniques used

The time-space variability of the annual-mean precipitation fields was decomposed using the EOF analysis package kindly provided by Aiguo Dai and used, for example, in Dai and Wigley (2000). EOF analysis can be performed using the raw data (and involving the computation of a covariance matrix) or using the raw data normalized by the local standard deviation (and involving the computation of a correlation matrix). The covariance matrix approach is used here so that the EOF patterns (or amplitudes) can be interpreted in terms of absolute rainfall amounts. The grid-point data are multiplied by the square root of the cosine of latitude prior to computing the EOFs.

Having computed the EOFs using the raw data, the EOF fields were divided by the maximum absolute value of the EOF field and the EOF amplitude coefficient was multiplied by the same factor. The amplitude coefficients thus have units of mm/day and can be interpreted as the maximum precipitation change associated with the corresponding EOF found anywhere at a given time.

## 3 Precipitation fields and variability

The model-simulated precipitation climatology is presented prior to discussing the results of the EOF analysis because the model precipitation climatology aids in the interpretation of the model EOF patterns and in understanding differences between the models in these patterns. As well, the model precipitation climatology serves as an indicator of the model performance in its own right.

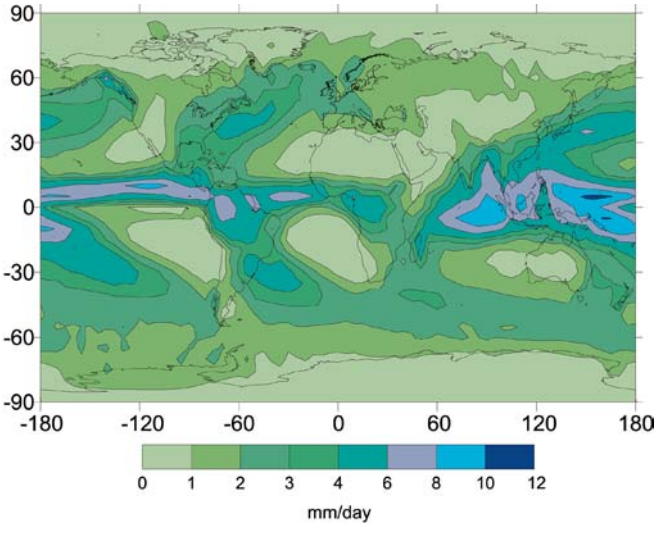


**Fig. 1** Annual-mean precipitation (mm/day) for the period January 1979–December 1999, according to the climatology of Xie and Arkin (1997)

### 3.1 Precipitation climatology

Figure 1 shows the annual-mean precipitation climatology as computed from the dataset developed by Xie and Arkin (1997). The Xie-Arkin (1997) data were obtained from the Web site http://www.cgd.ucar.edu/cas/catalog/surface/precip/arkin.html, directory /pub/precip/cmap/monthly, and had been updated to contain global precipitation fields for each month during the 21-year period January 1979–December 1999. This dataset is based on a combination of rain gauge measurements, satellite data, and NCAR-NCEP reanalysis data. Figure 2 shows the annual-mean precipitation averaged over the control run for each of the AOGCMs. The observed precipitation field contains a well-defined east-west band of high precipitation across the entire Pacific Ocean and centered at about 10°N (associated with the Intertropical

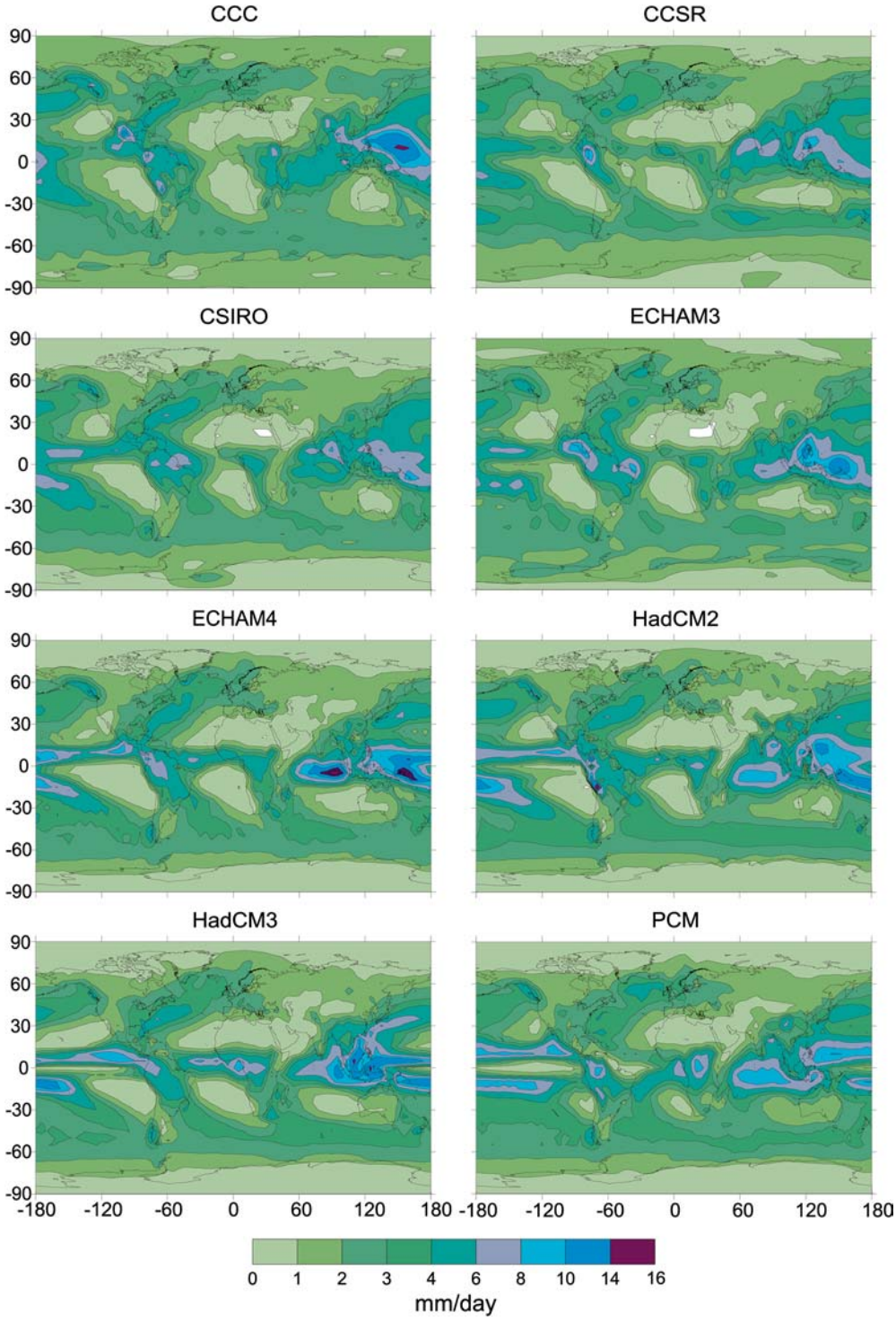


**Fig. 2** Annual-mean control-run precipitation (mm/day) for the eight models

Convergence Zone, ITCZ), a second NW-SE band across the south Pacific (associated with the South Pacific Convergence Zone, SPCZ), and precipitation maxima over the Pacific Ocean to the NNE of New Guinea, over the Indian Ocean to the west of Indonesia, over the western Amazon basin, over central Africa, and at various locations in midlatitudes. Some models fail to simulate a Pacific-wide precipitation maximum associated with the ITCZ (CCC, CCSR, ECHAM3) or represent the SPCZ poorly (CCSR, ECHAM3, HadCM3, PCM). CSIRO, ECHAM4, and HadCM2 do well in simulating both the Pacific ITCZ and SPCZ. The two non-flux-adjusted models (HadCM3 and, especially, PCM) have a double ITCZ structure in the Pacific sector, rather than a single ITCZ north of the equator. All of the models at least crudely simulate the correct placement of the other precipitation maxima.

**Table 2** Pattern correlation ($R^2$) between model and observed precipitation climatology and the first precipitation EOF, and standard deviation of model and observed amplitude of annual $EOF_1$ (seasonal standard deviations are given in Fig. 9a)

| Model | Pattern correlations between model and observations | | | | | | | | Standard deviation of annual EOF amplitude |
|---|---|---|---|---|---|---|---|---|---|
| | Climatology | | | $EOF_1$ | | | | | |
| | Annual | DJF | JJA | Annual | DJF | MAM | JJA | SON | |
| CCC | 0.61 | 0.62 | 0.51 | 0.26 | 0.23 | 0.04 | 0.01 | 0.10 | 1.61 |
| CCSR | 0.66 | 0.64 | 0.61 | 0.45 | 0.29 | 0.23 | 0.24 | 0.29 | 1.91 |
| CSIRO | 0.80 | 0.75 | 0.64 | 0.36 | 0.01 | 0.00 | 0.10 | 0.07 | 0.83 |
| ECHAM3 | 0.75 | 0.69 | 0.65 | 0.48 | 0.13 | 0.06 | 0.31 | 0.25 | 1.68 |
| ECHAM4 | 0.85 | 0.81 | 0.72 | 0.12 | 0.24 | 0.30 | 0.41 | 0.31 | 3.33 |
| HadCM2 | 0.81 | 0.82 | 0.75 | 0.61 | 0.50 | 0.29 | 0.41 | 0.49 | 2.68 |
| HadCM3 | 0.79 | 0.79 | 0.74 | 0.15 | 0.21 | 0.48 | 0.10 | 0.18 | 2.81 |
| PCM | 0.56 | 0.56 | 0.49 | 0.19 | 0.06 | 0.08 | 0.20 | 0.12 | 1.69 |
| Observed | | | | | | | | | 2.88 |
| Range of $R^2$ correlations between models | 0.42–0.82 | 0.37–0.79 | 0.39–0.72 | 0.00–0.59 | 0.00–0.56 | 0.00–0.60 | 0.00–0.49 | 0.00–0.63 | |

Table 2 gives the pattern correlations ($R^2$) between the observations and the models for annual-mean, December–January–February (DJF), and June–July–August (JJA) precipitation. As in Part 1, the individual data points are weighted by the square root of the cosine of latitude. $R^2$ values for annual-mean precipitation range from 0.56 to 0.85. DJF values tend to be slightly smaller, while JJA values are consistently smaller than the annual-mean values. The better correlations for annual-mean precipitation are not surprising, given that errors in the timing of precipitation (which can affect seasonal correlations) will cancel in the annual mean. As discussed in Part 1, all models do very well in simulating the observed annual-mean climatological temperature fields, with $R^2$ values ranging from 0.96 to 0.99. For all except HadCM3 and PCM, this is due in part to the use of flux adjustment. The correlations between the models and observations tend to be larger than the correlations among the models themselves, an encouraging result. The model-observed correlations for the non flux-adjusted models are similar to the correlations obtained for the flux-adjusted models.

Figure 3 compares the latitudinal variation in the annual-mean, zonally averaged precipitation as simulated by the eight models, and lower and upper bounds of the observed precipitation (accounting for uncertainties) as given in the Xie-Arkin dataset. All of the models generally fall within the observational envelope, the only noticeable exceptions being CCC, which appears to simulate slightly too much precipitation poleward of about 40°N, and PCM near 15°S. The latter is a reflection of the aforementioned double ITCZ structure.

## 3.2 Precipitation EOFs

Figure 4 shows $EOF_1$ of the annual-mean precipitation data of Xie and Arkin (1997). This EOF is similar to that of Dai and Wigley (2000), which was computed based on an expanded dataset that includes the Xie-Arkin data, supplemented with additional data from 1900–1978. The

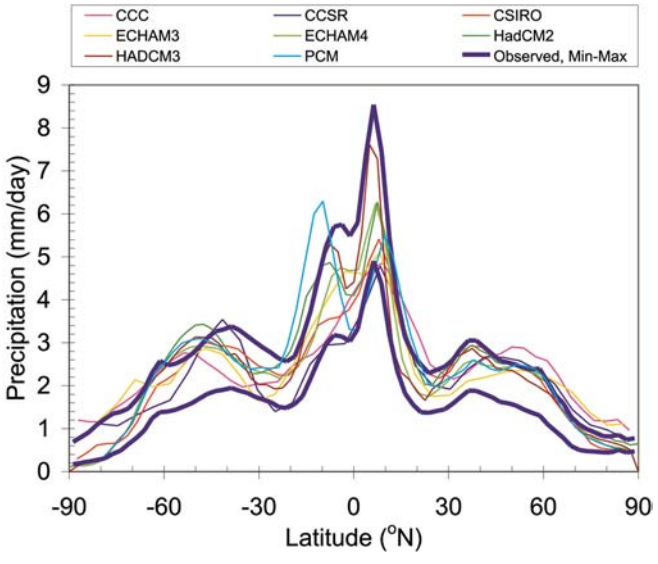


**Fig. 3** Zonal annual-mean control-run precipitation (mm/day) for the eight models and for observations

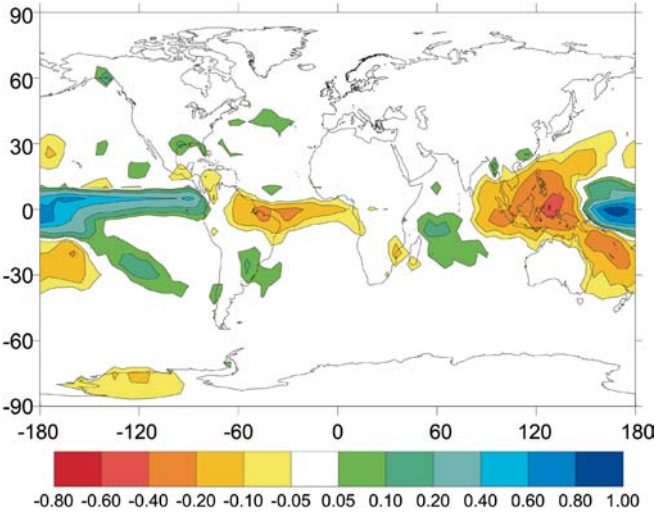


**Fig. 4** The first EOF (dimensionless) of observed annual-mean precipitation

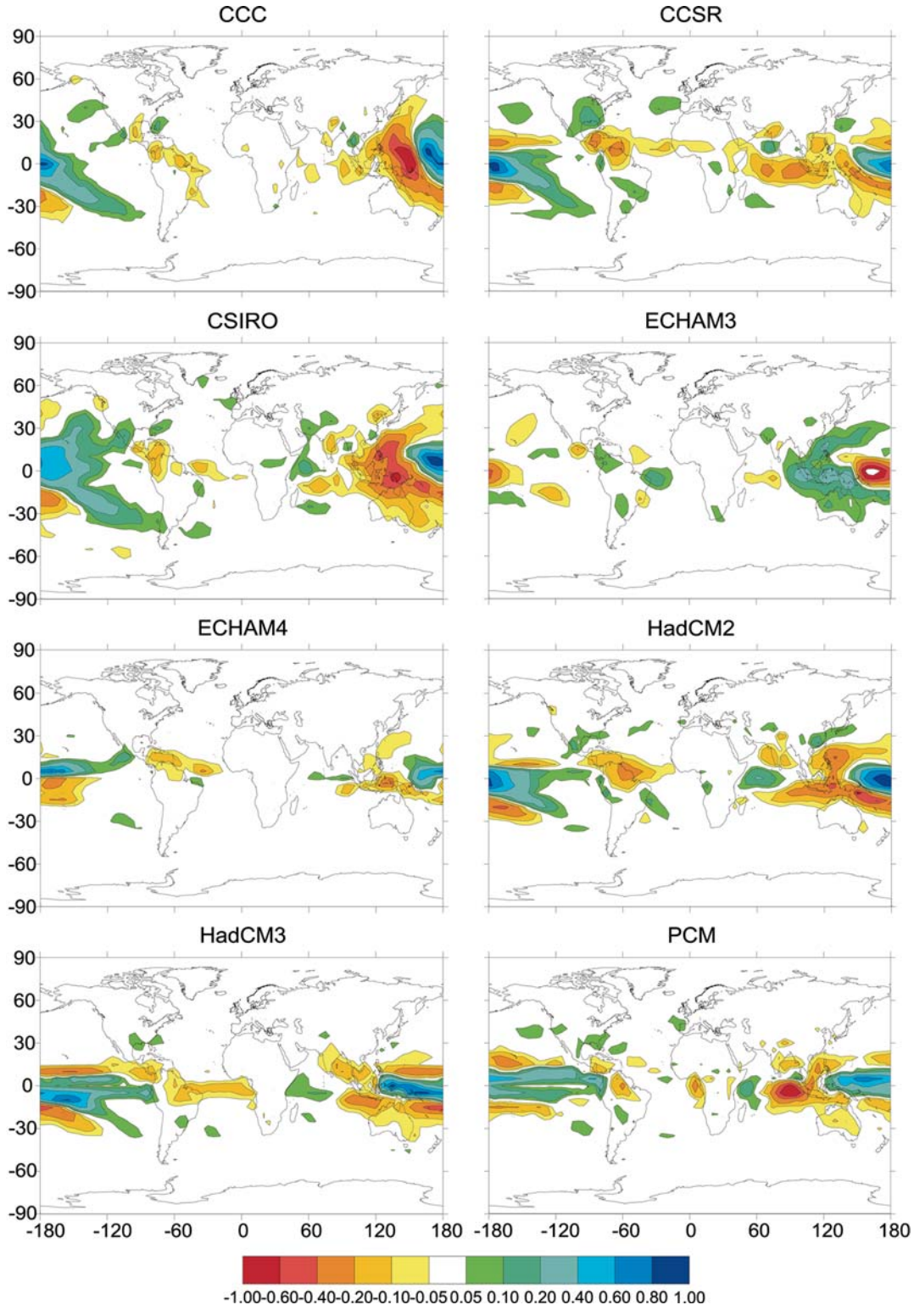


**Fig. 5** The first EOF (dimensionless) for the eight models, based on annual-mean precipitation

first EOF is clearly associated with ENSO variations. There are strong bands of positive precipitation anomaly along the Pacific Ocean ITCZ and SPCZ. One prominent offsetting negative anomaly occurs from French Caledonia, through northern Australia, New Guinea, and Indonesia, to the east cost of India. A second prominent negative anomaly occurs from the Brazilian Amazon across the Atlantic Ocean to equatorial central Africa.

Figure 5 shows $EOF_1$ for annual-mean precipitation for all eight AOGCMs. As in the observations, it is

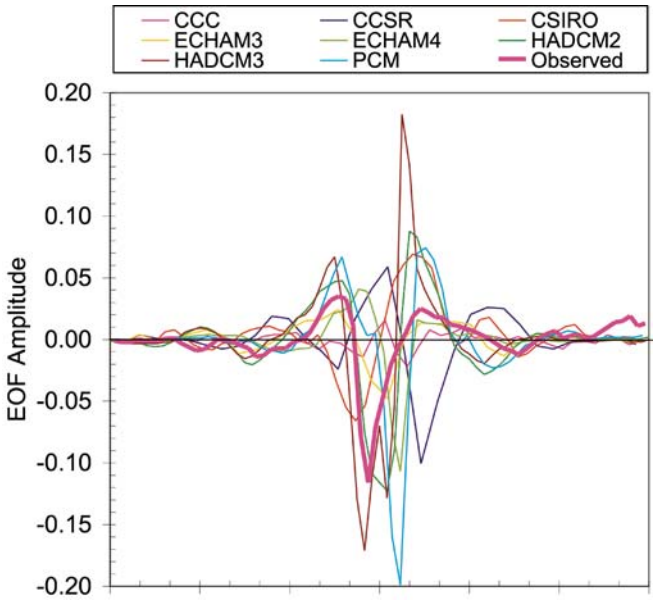


**Fig. 6** Zonal-mean values of the first EOF (dimensionless) for the eight models and for observations

dominated by strong, closely spaced anomalies of opposite sign in the western equatorial Pacific Ocean, associated with an east-west shift in the region of maximum precipitation to the north of New Guinea that in turn is tied to the Walker circulation and the El Niño oscillation. Errors in the model $EOF_1$ field are generally associated with errors in the climatology. For example, CCC, CCSR, CSIRO, and ECHAM3 all fail to show a trans-Pacific maximum in $EOF_1$, and also fail to show a strong trans-Pacific ITCZ in the precipitation climatology. ECHAM3 and PCM fail to show the SPCZ in $EOF_1$ and in the precipitation climatology. On the other hand, CSIRO has a good ITCZ in the climatology but not in $EOF_1$. In two models (HadCM3 and PCM) the boundary between positive and negative anomalies in the western equatorial Pacific Ocean is too far west (a result previously reported by Meehl et al. (2001) for the PCM). HadCM3 is the only model in which the negative precipitation anomaly over northeastern Brazil and the equatorial Atlantic is well represented.

Figure 6 compares the zonal mean of $EOF_1$ for the models and for observations. None of the models comes even close to simulating the correct zonal-mean values. CCC shows too small a zonal-mean $EOF_1$ value because of partial cancellation of the precipitation anomalies due to the anomalies having too much of a north-south rather than east-west orientation. In the case of HadCM3, on the other hand, the zonal-mean values are much too large because the precipitation anomalies are too strongly oriented east-west. The other models fall between these two extremes.

Table 2 gives the $R^2$ correlations between model and observed $EOF_1$ for annual-mean and seasonal precipitation. Correlations range from 0.12 to 0.61 for annual-mean $EOF_1$, and are almost always lower for seasonal EOFs. Most of the models do better in simulating observed precipitation $EOF_1$ then temperature $EOF_1$; the exceptions are ECHAM4, HadCM3, and PCM, in which the $R^2$ correlation for precipitation $EOF_1$ is relatively low. For some model-model comparisons, the correlation between models is better than the correlation between any of the models and the observations. Figure 7 shows the seasonal $EOF_1$ fields for the observations and for models having low (CSIRO) and high (HadCM2) correlations with observed $EOF_1$ on a seasonal basis. Cases of poor pattern correlation, even as low as 0.0, seem to arise more from a misplacement in the centers of the major positive and negative features, or errors in their extent, rather than from their absence.

The last column of Table 2 compares the standard deviation of the model and observed amplitudes for annual $EOF_1$. HadCM2 and HadCM3 have about the right amplitude for $EOF_1$, ECHAM4 too large an amplitude, and the other models too small an amplitude. Figure 8 shows the percentage of space-time annual-mean variance explained by $EOF_1$ for all eight models and for the observations. These are complementary measures of the importance of $EOF_1$, as the variation in the amplitude is related to the magnitude of variability at the strongest center of action, while the explained variance is related to how much of the global space-time variation is related to the EOF. $EOF_1$ accounts for a low of 10–12% of total space-time variation in four of the models, and a high of 26% in the case of HadCM3. The latter compares well with the observed value of 29%. (NB In Dai and Wigley (2000), $EOF_1$ accounts for only 5.5% of the total variation. Unlike us, they normalized the raw data by the interannual standard deviation before computing the EOFs. Normalization by the standard deviation increases the signal strength for precipitation at higher latitudes, so that modes of variability tied to the tropics are less important to the global variability.) Figure 9 shows how the models compare with observations for these two measures on a seasonal basis. In the observations, the amplitude of $EOF_1$ is most variable during DJF, while the percent of total space-time variation accounted for by $EOF_1$ is distinctly greater during the transition seasons (March–April–May, MAM, and September–October–November, SON) than during DJF and JJA. None of the models show a DJF maximum in the amplitude variation, and only two models (HadCM2 and HadCM3) show distinct MAM and SON maxima in accounted-for variability.

## 4 Correlation between precipitation EOF amplitudes and pressure indices

Harvey and Wigley (2003) interpreted the observed and model temperature quasi-$EOF_2$ as representing ENSO. They found that the correlation between the model Southern Oscillation Index (SOI) and the temperature q$EOF_2$ amplitude is comparable to (or slightly larger than) the correlation between the observed SOI and

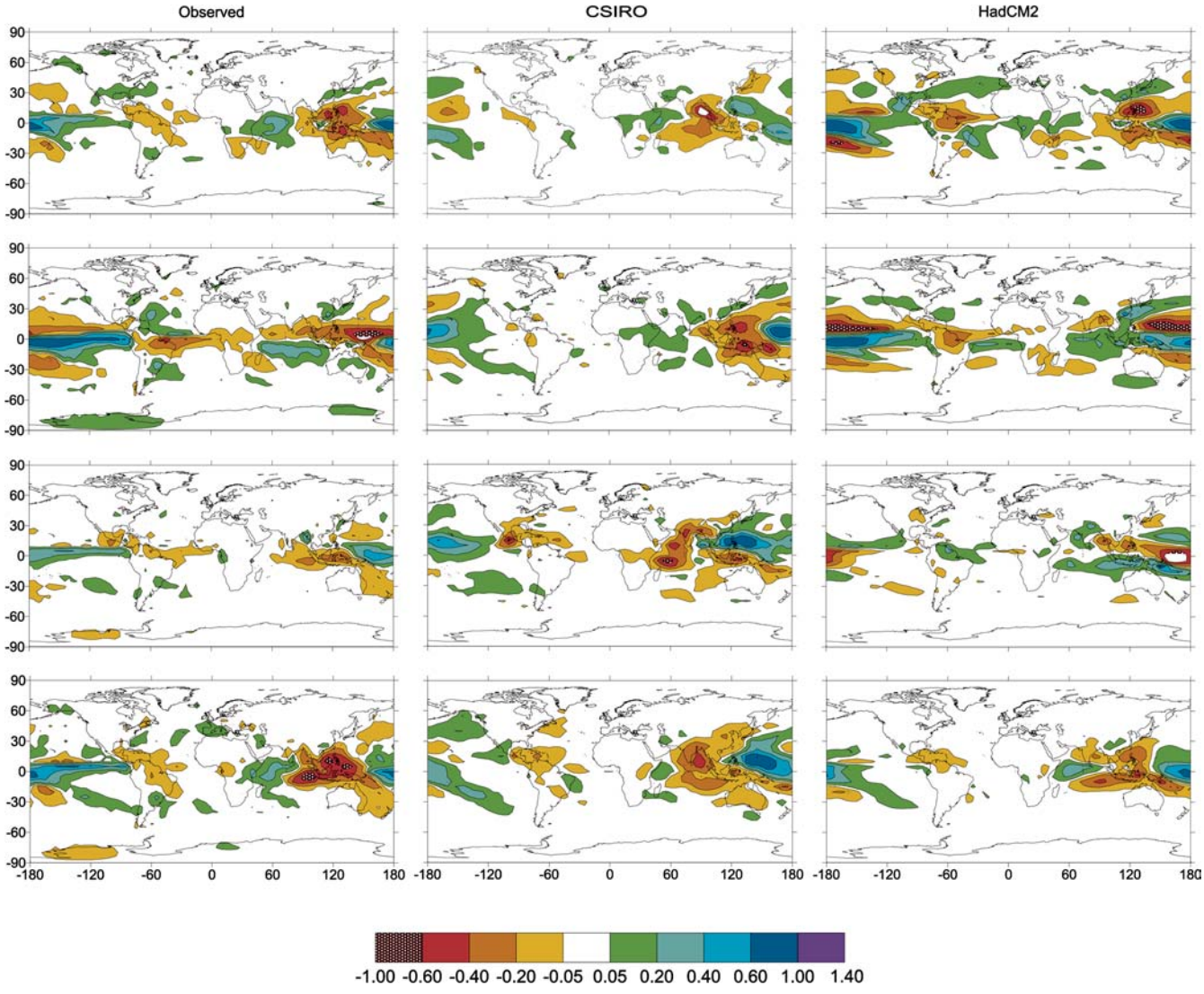


**Fig. 7** The first EOF (dimensionless) for each season for the observations, the CSIRO model, and the HadCM2 model. From *top* to *bottom*: DJF, MAM, JJA, SON

$qEOF_2$ amplitude in four of the models, but distinctly lower in the other four models. However, if an alternative SOI that maximizes the correlation with the amplitude of temperature $qEOF_2$ is used, then correlations comparable to that observed are found in all models. This implies that in the four models with initially low correlation, the low correlations are a result of the centers of pressure variability being displaced from observed centers. One might expect that these errors are in turn related to errors in the climatological SST field. If this is so, the effect is rather subtle, because in the models without flux adjustment (HadCM3 and PCM), there are larger errors in the SST fields (see Part 1). This does not, however, lead to poorer SOI/precipitation-$qEOF_1$ correlations.

Here, the time series correlations between the SOI and precipitation $EOF_1$ amplitudes for the models and for observations are compared. The standard SOI is given by the surface pressure at Tahiti minus the surface pressure at Darwin (Australia). As in Part 1, time series of observed monthly mean pressure at both locations that are available from the website of the Climate Research Unit of the University of East Anglia (http://www.cru.uea.ac.uk) are used. Also as in Part 1,625 alternative SO indices were generated from all possible combinations of differences between the pressure at 25 grid points surrounding (and including) the grid points containing Tahiti and Darwin. This accounts for the possibility that the models have pressure variability comparable to observed, but with somewhat displaced centers of action. In Part 1, the standard SOI and the alternative SOI having the maximum correlation with the amplitude of temperature $qEOF_2$ were considered. Here, there are three choices: the standard SOI, the SOI with maximum correlation with the amplitude of temperature $qEOF_2$, or the SOI with maximum correlation with the amplitude of precipitation $EOF_1$. Although the grid points for the latter two SOIs are often different,

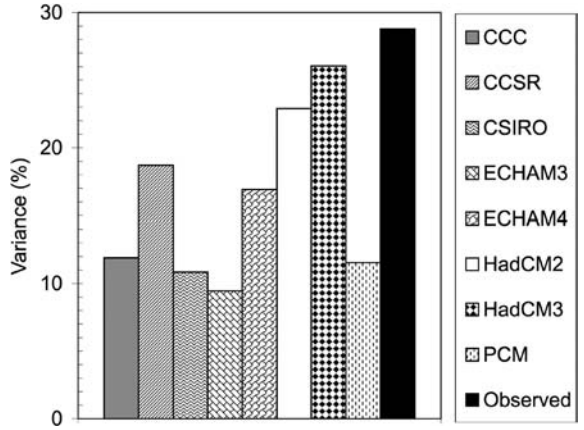


**Fig. 8** Percentage of the total precipitation annual-mean space-time variation that is accounted for by the first EOF for the eight models and for observations

**Table 3** Correlation ($R^2$) between the SOI and the amplitude of temperature $qEOF_2$ (from Harvey and Wigley 2003) and the amplitude of precipitation $EOF_1$. In both cases, results are given using the standard SOI and (in brackets) using the alternative SOI that maximizes the correlation with the $qEOF_2$ amplitude time series. Also given is the correlation ($R^2$) between the amplitude of temperature $qEOF_2$ and precipitation $EOF_1$

| | Correlation of the SOI with | | Correlation between temperature $qEOF_2$ and precipitation $EOF_1$ |
|---|---|---|---|
| | Temperature $qEOF_2$ | Precipitation $EOF_1$ | |
| CCC | 0.67 (0.79) | 0.74 (0.87) | 0.74 |
| CCSR | 0.29 (0.74) | 0.38 (0.85) | 0.79 |
| CSIRO | 0.52 (0.70) | 0.62 (0.81) | 0.63 |
| ECHAM3 | 0.22 (0.72) | 0.17 (0.81) | 0.50 |
| ECHAM4 | 0.49 (0.69) | 0.17 (0.44) | 0.39 |
| HadCM2 | 0.67 (0.77) | 0.83 (0.90) | 0.81 |
| HadCM3 | 0.52 (0.75) | 0.51 (0.82) | 0.69 |
| PCM | 0.34 (0.63) | 0.28 (0.48) | 0.72 |
| Observed | 0.61 | 0.82 | 0.84 |

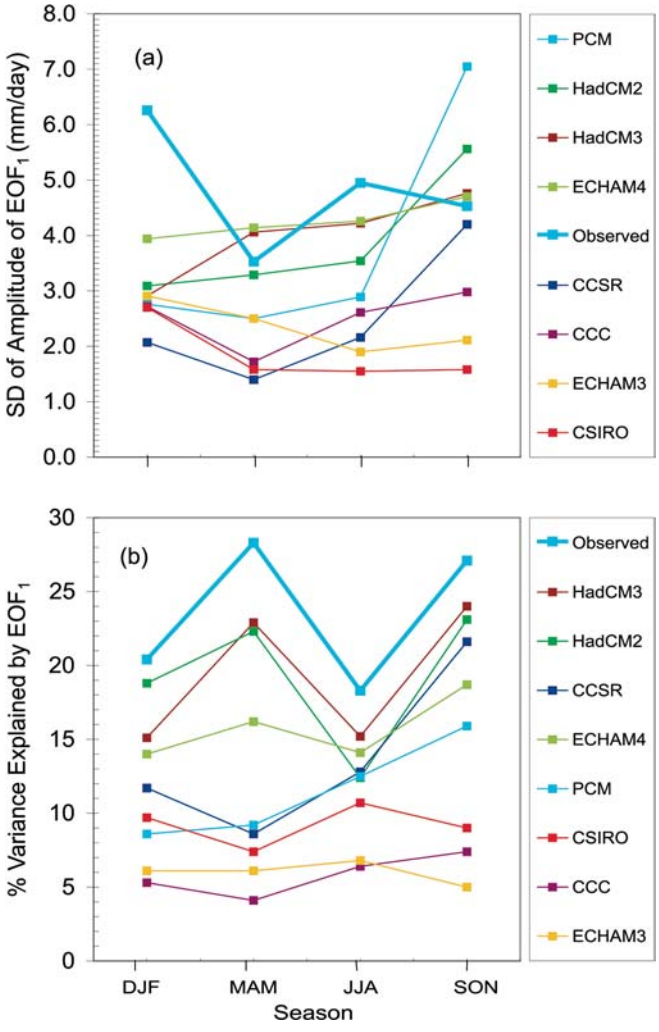


**Fig. 9** **a** The standard deviation of the amplitude of the first EOF for each season (mm/day). **b** The fraction of total seasonal space-time variation that is accounted for by the first EOF for the eight models and for observations

there is little difference in the results to be presented later. Thus, for each model, the correlation between the SOI and the precipitation $EOF_1$ amplitude is presented for the alternative SOI that has the largest correlation with the amplitude of temperature $qEOF_2$. This will be referred to as the preferred alternative SOI.

Results are given in Table 3, using observed data for the period 1979–1999 and for the entire control-run in the case of model data. Using the standard SOI, the $R^2$ correlations with the amplitude of precipitation $EOF_1$ range from 0.17 (ECHAM3 and ECHAM4) to 0.82 (HadCM2), compared to an observed correlation of 0.83. Using the preferred alternative SOI, the maximum correlation ranges from 0.44 to 0.90, with all except two models having correlations comparable to or somewhat greater than observed. The model and observed correlations are generally better for precipitation than for temperature, which are given in Part 1 and again in Table 3 for the reader's convenience. This is reasonable, given that precipitation is more directly related to pressure patterns than is temperature.

The standard SOI-$EOF_1$ correlations obtained here are similar to those reported by Doherty and Hulme (2002) for the same models as analyzed here. Their analysis differs from the one presented here, however, in that they computed EOFs over the domain 30°S–30°N rather than over the global domain, they used years extending from June to May, and they analyzed the period 1900–1949 of the greenhouse gas-increase run rather than the 200–240 years of the control run.

The last column of Table 3 gives the $R^2$ correlation between the amplitude of precipitation $EOF_1$ and temperature $qEOF_2$; many of the models compare well with the observed correlation of 0.84. Recall that temperature $qEOF_2$ is computed based on the correlations of local temperature with temperature variations in the Niño 3 region. It is thus predisposed to produce a pattern of temperature variability that should be linked to ENSO.

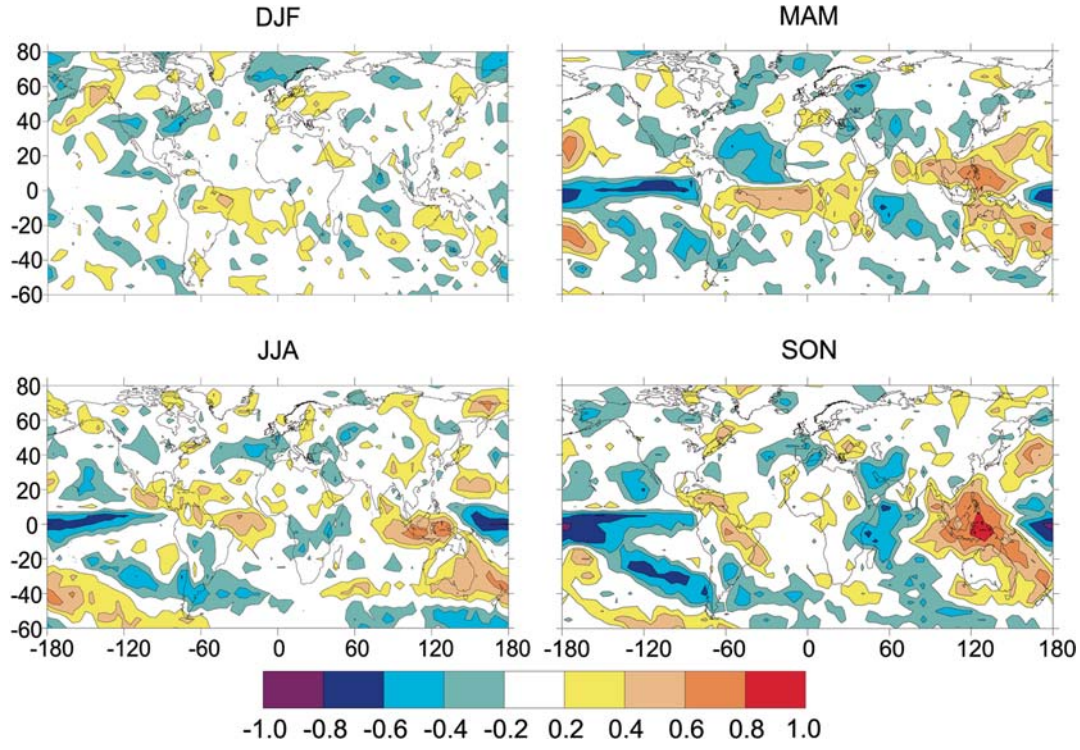


**Fig. 10** Spatial variation of the observed temporal correlation between local precipitation and the SOI. Results are given for seasonally averaged precipitation and SOI values

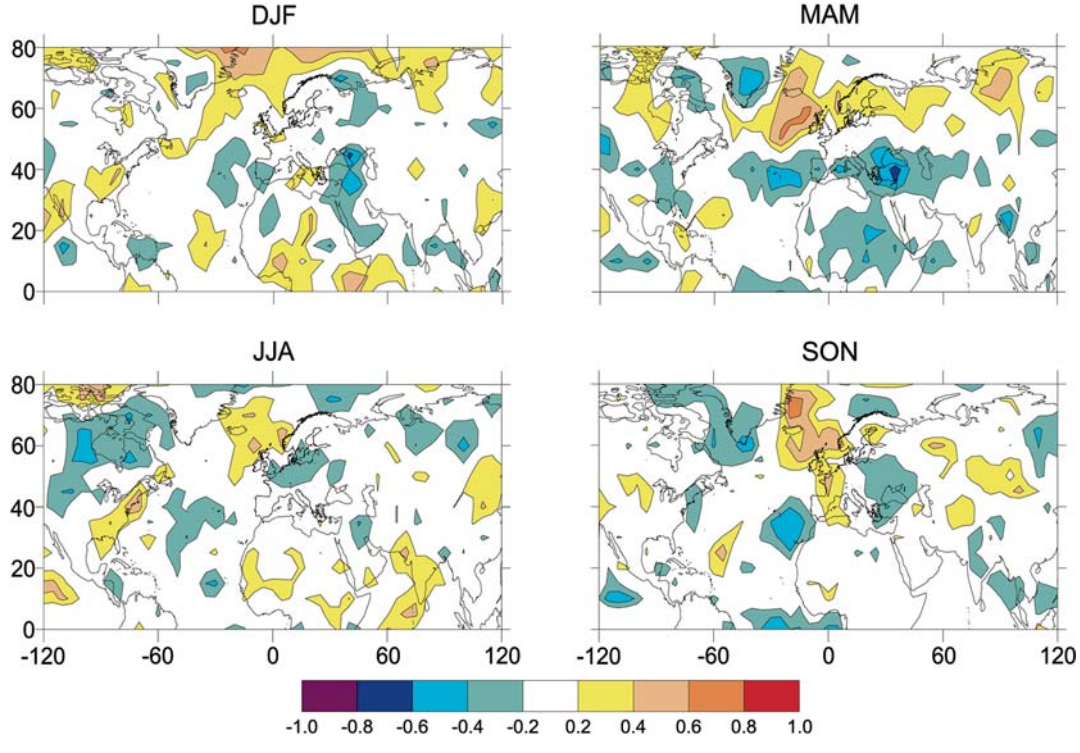


**Fig. 11** Spatial variation of the observed temporal correlation between local precipitation and the NAOI. Results are given for seasonally averaged precipitation and NAOI values

As a final comparison between model and observed precipitation variability, the spatial variation in the local correlation between precipitation and the SOI, and between precipitation and the North Atlantic Oscillation Index (NAOI) is examined. The NAOI is defined as the surface pressure at Gibralter minus that at Reykjavik,

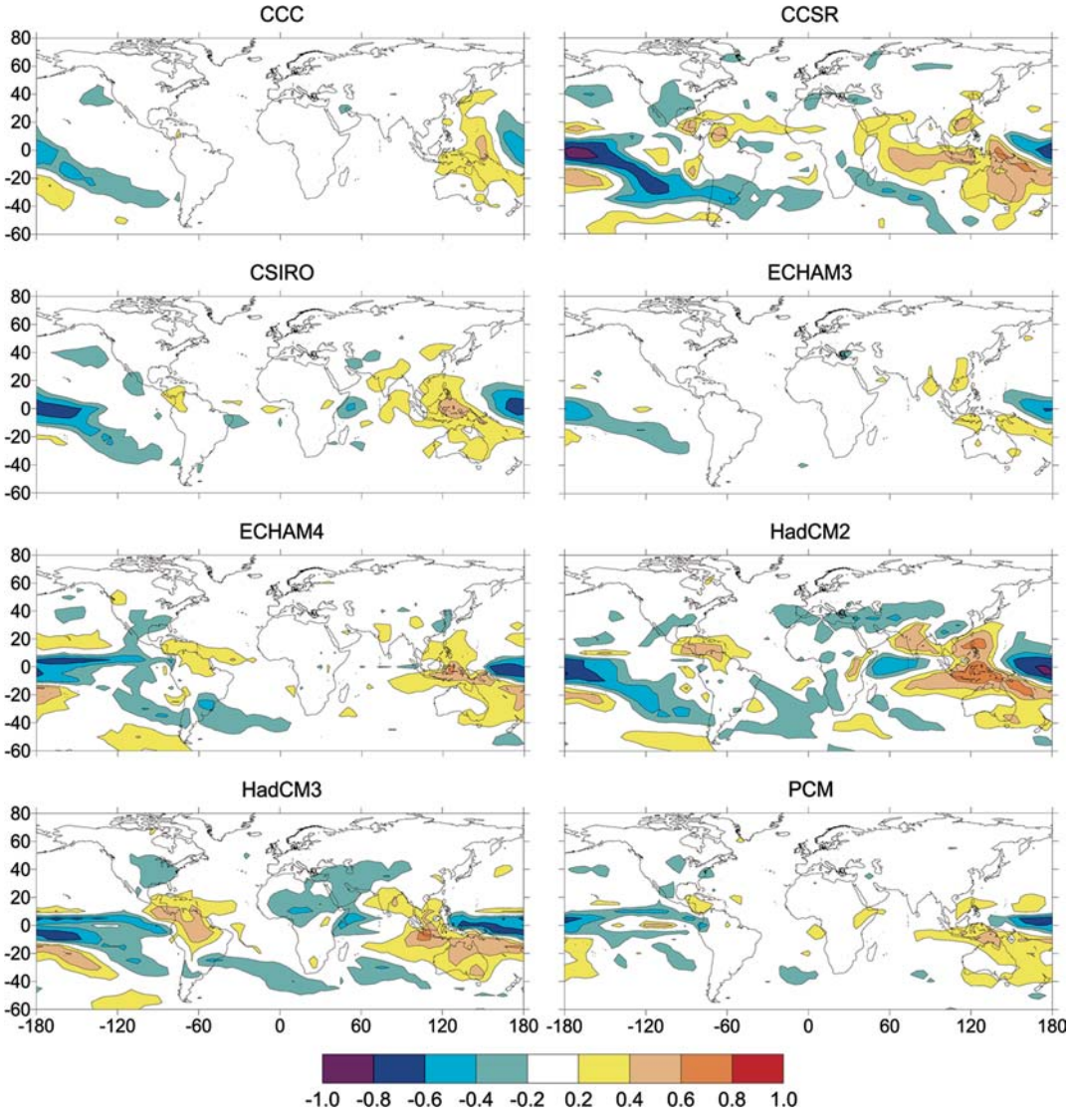


**Fig. 12** Spatial variation of the temporal correlation between local SON precipitation and the preferred alternative SOI for the eight models

Iceland, observed values of which were obtained from the afore-mentioned CRU website. Figures 10 and 11 show the fields of the observed correlation with the SOI and NAOI, respectively, for each season. For the SOI and NAOI, the strongest areally-averaged correlations are seen in SON and MAM, respectively, so model fields are given in Fig. 12 for the SON SOI correlation only, and in Fig. 13 for the MAM NAOI correlation only. For the SOI, stronger correlations with local precipitation are obtained using the preferred alternative index, while for the NAOI, the standard index produces slightly stronger correlations than alternative NAO indices (see Part 1). For this reason, Fig. 12 gives the correlation between local precipitation and the preferred alternative SOI, while Fig. 13 gives the correlation between local precipitation and the standard NAOI.

The seasonal SOI correlation patterns strongly resemble the seasonal $EOF_1$ fields, as can be seen for CSIRO and HadCM2 for SON by comparing Figs. 7 and 12. As for the NOAI, precipitation in southern Europe and (more-so) the adjoining Atlantic Ocean is negatively correlated with the NAOI, while precipitation in northwestern Europe and the adjoining Atlantic Ocean is positively correlated with the NAOI, both in the observations (Fig. 11) and models (Fig. 13).

## 5 Discussion and concluding comments

In this work the variability of annual-mean precipitation in eight AOGCMs and in observations has been examined. The leading EOF of precipitation variability in both models and observations is centered around the low-latitude western Pacific Ocean and Indian Ocean, and is related to ENSO. Pattern correlations between the model and observed $EOF_1$ range from 0.12 to 0.61.

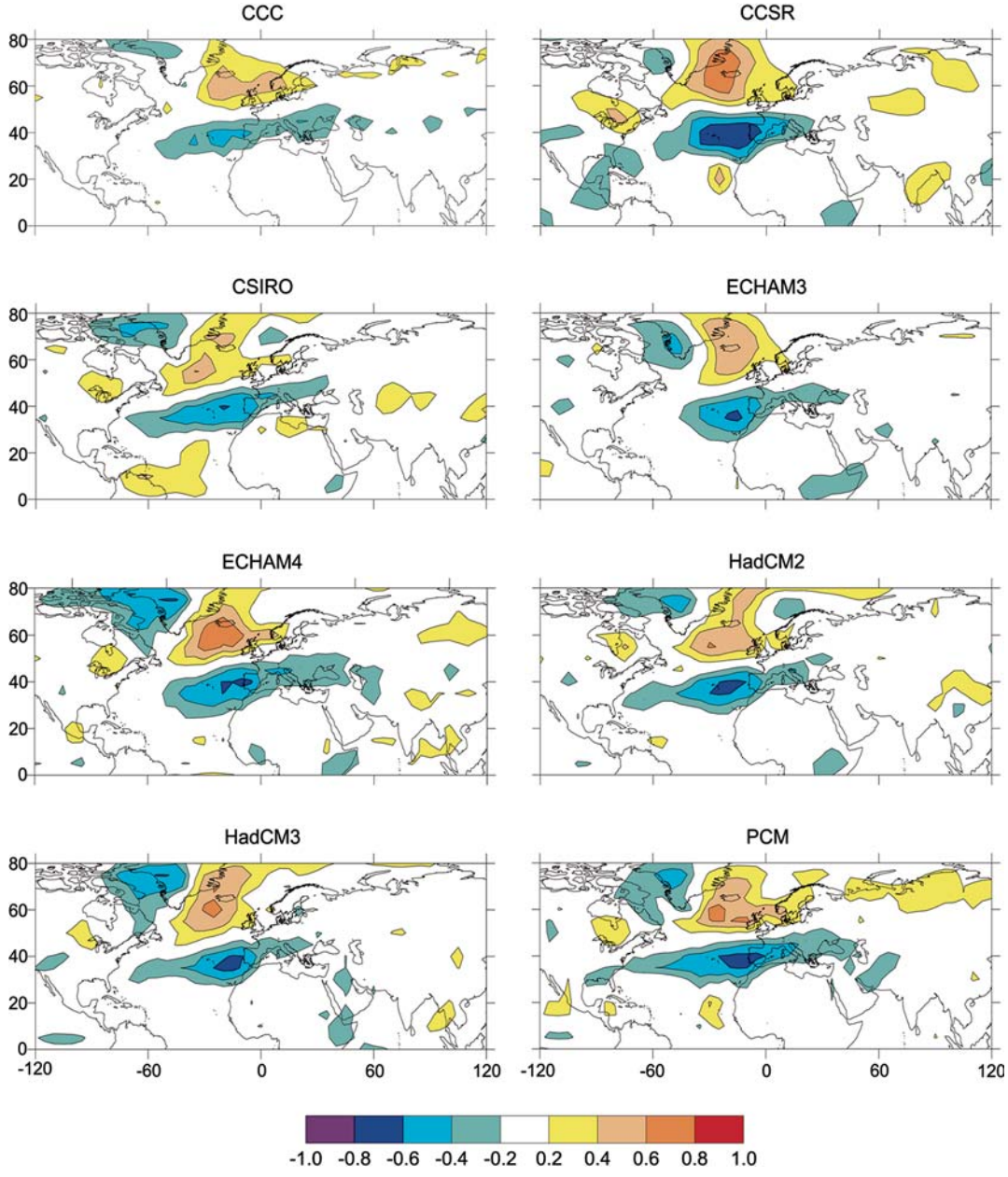


**Fig. 13** Spatial variation of the temporal correlation between local MAM precipitation and the standard DJF NAOI for the eight models

Errors in the $EOF_1$ field are generally related to errors in the climatological field, so improvement in the model climatology should lead to a better representation of interannual variability. The SOI is highly correlated with the amplitude of precipitation $EOF_1$ in both models and observations, although for some models an alternative SOI needs to be considered to allow for displaced centers of pressure variability in the models. Maps of the correlation between local precipitation and the SOI resemble the $EOF_1$ fields, and the correlation maps for both the SOI and NAOI for the models show many of the features seen in the observations.

There are, nevertheless, many instances where the model simulation of precipitation and precipitation variability needs to be improved. These include the structure of the climatological rainbelts and variability at low latitudes in most of the models. The simulation of changes in precipitation is critical to the impacts of increasing greenhouse gas concentrations. Changes in precipitation are likely to be more important than changes in temperature for the impacts of climatic change on tropical forests. HadCM3, for example, projects that almost the entire Amazon rainforest is replaced by semi-desert due to a drastic reduction in rainfall in the Amazon basin in association with a global-mean warming of about 3.3 °C (White et al. 1999). In HadCM2, the Amazon rainforest is still largely intact by 2100 (when the simulation ends) but with greatly

reduced productivity, and a positive climate-carbon cycle feedback has caused a significant enhancement in the buildup of atmospheric $CO_2$ (Cox et al. 2000). For this reason, improving the simulation of precipitation and precipitation variability in climate models is critically important.

**Acknowledgements** This work was supported by NSERC grant OPG0001413. Constructive comments on an earlier version by two reviewers are appreciated

## References

Bacher A, Oberhuber JM, Roeckner, E (1998) ENSO dynamics and seasonal cycle in the tropical Pacific as simulated by the ECHAM4/OPYC3 coupled general circulation model. Clim Dyn 14: 431–450

Collins M, Tett SFB, Cooper C (2001) The internal climate variability of HadCM3, a version of the Hadley Centre coupled model without flux adjustments. Clim Dyn 17: 61–81

Cox PM, Betts RA, Jones CD, Spall SA, Totterdell IJ (2000) Acceleration of global warming due to carbon-cycle feedbacks in a coupled climate model. Nature 408: 184–187

Dai A, Wigley TML (2000) Global patterns of ENSO-induced precipitation. Geophys Res Lett 27: 1283–1286

Doherty R, Hulme M (2002) The relationship between the SOI and extended tropical precipitation in simulations of future climate change. Geophys Res Lett 29 (10): 113, DOI 10.1029/2001GL014601

Emori S, Nozawa T, Abe-Ouchi A, Numaguti A, Kimoto M, Nakajima T (1999) Coupled ocean–atmosphere model experiments of future climate change with an explicit representation of sulfate aerosol scattering. J Meteorol Soc Japan 77: 1299–1307

Flato GM, Boer GJ, Lee WG, McFarlane NA, Ramsden D, Reader MC, Weaver AJ (2000) The Canadian Centre for Climate Modelling and Analysis Global Coupled Model and its climate. Clim Dyn 16: 451–467

Gordon HB, O'Farrell SP (1997) Transient climate change in the CSIRO coupled model with dynamic sea ice. Mon Weather Rev 125: 875–907

Gordon C, Cooper C, Senior CA, Banks H, Gregory JM, John, TC, Mitchell JFB, Wood RA (2000) The simulation of SST, sea ice extents and ocean heat transports in a version of the Hadley Centre coupled model without flux adjustments. Clim Dyn 16: 147–168

Harvey LDD, Wigley TML (2003) Characterizing and comparing control-run variability of eight coupled AOGCMs and of observations. Part 1: temperature. DOI 10.1007/s00382-003-0357-x

Johns TC, Carnell RE, Crossley JF, Gregory JM, Mitchell JFB, Senior CA, Tett SFB, Wood RA (1997) The second Hadley Centre coupled ocean–atmosphere GCM: model description, spinup and validation. Clim Dyn 13: 103–134

Meehl GA, Gent P, Arblaster JM, Otto-Bliesner B, Brady E, Craig A (2001) Factors that affect amplitude of El Niño in global coupled climate models. Clim Dyn 17: 515–526

Tett SFB, Johns TC, Mitchell JFB (1997) Global and regional variability in a coupled AOCGM. Clim Dyn 13: 303–323

Timmermann A, Latif M, Grötzner A, Voss R (1999) Modes of climate variability as simulated by a coupled general circulation model. Part I: ENSO-like climate variability and its low-frequency modulation. Clim Dyn 15: 605–618

Walland DJ, Power SB, Hirst AC (2000) Decadal climate variability simulated in a coupled general circulation model. Clim Dyn 16: 201–211

Washington WM, Weatherly JW, Meehl GA, Semtner AJ, Bettge TW, Craig AP, Strand WG, Arblaster JM, Wayland VB, James R, Zhang Y (2000) Parallel climate model (PCM) control and transient simulations. Clim Dyn 16: 755–774

White A, Melvin GRC, Friend AD (1999) Climate change impacts on ecosystems and the terrestrial carbon sink: a new assessment. Glob Env Change 9: S21–S30

Xie P, Arkin PA (1997) Global precipitation: a 17-year monthly analysis based on gauge observations, satellite estimates and numerical model outputs. Bull Am Meteorol Soc 78: 2539–2558